Mass to light ratio of galaxies and gravitational lensing [*]

Nan Li, Ran Li and Xin-Zhong Er

National Astronomical Observatories, Chinese Academy of Sciences, Beijing 100012, China;
uranus@bao.ac.cn

Abstract We investigate the potential of constraining the mass to light ratio of field galaxies using weak lensing shear and flexions. A suite of Monte Carlo simulations are used to generate weak lensing observations with different noise models. Using mock data, we find that the inclusion of flexions can improve the estimate of foreground halo parameters, but the details are strongly dependent on noise in the model. In the intrinsic noise limit, both shear and flexions are promising tools to study the mass to light ratio of galaxies. However, if the noise model of flexions follows the form described by Rowe et al., there is only $\sim 5\%$ improvement in the constraints even with next generation lensing observations.

Key words: cosmology: dark matter — galaxies: halos — gravitational lensing

1 INTRODUCTION

According to the paradigm of standard galaxy formation in a cold dark matter universe, dark matter halos grow hierarchically through merging and accretion. Cold gas condenses in the potential well of dark halos, forming galaxies (White & Rees 1978; White & Frenk 1991). The key challenge in this field is to understand how galaxies with different observed properties populate dark matter halos. Theoretically, the connection between dark halos and galaxies can be investigated with numerical simulations (e.g. Katz et al. 1996; Pearce et al. 2000; Springel 2005) and semi-analytical models (e.g. White & Frenk 1991; Kauffmann et al. 1993, 2004; Somerville & Primack 1999; Cole et al. 2000; van den Bosch et al. 2002; Kang et al. 2005; Croton et al. 2006; Guo et al. 2011). Although the evolution of dark matter structure is dominated by gravitation, galaxy formation involves more complicated physics, such as radiative cooling, star formation and feedback, much of which are still poorly understood. Thus, it is essential to test theoretical predictions using observations.

Gravitational lensing, which measures image distortions of background galaxies caused by the foreground gravitational field, is considered to be one of the most promising tools to investigate the dark matter distribution. In particular, galaxy-galaxy weak lensing, which focuses on the image distortions around selected foreground galaxies, provides a direct measurement of the correlation between a galaxy and its associated dark matter (e.g. Mandelbaum et al. 2005, 2006; Yang et al. 2006; Cacciato et al. 2009; Li et al. 2009, 2013). Because the galaxy-galaxy lensing effect around individual galaxies is too weak to be detected, stacking is widely used to extract useful information about lens galaxies. Tyson et al. (1984) made the first attempt to detect galaxy-galaxy lensing effects. More recently, with the advent of large galaxy surveys, galaxy-galaxy lensing has been studied for

lens galaxies with different luminosities, stellar masses, colors and morphologies (e.g. Brainerd et al. 1996; Hudson et al. 1998; McKay et al. 2001; Hoekstra et al. 2003, 2004; Sheldon et al. 2004; Mandelbaum et al. 2005, 2006; Johnston et al. 2007; Mandelbaum et al. 2008; Velander et al. 2011; Kilbinger et al. 2013; Gillis et al. 2013; Simon et al. 2013; Heymans et al. 2013). These results provide important constraints on the relation between a galaxy and dark matter using statistical methodology.

Most galaxy-galaxy weak lensing studies utilize shear, which is the first-order distortion of the lensed image. It transforms a circular image into an elliptical one. Gravitational flexions have recently been proposed to investigate dark matter distributions (e.g. Goldberg & Bacon 2005; Bacon et al. 2006; Leonard et al. 2007; Schneider & Er 2008; Hawken & Bridle 2009; Er 2012; Velander et al. 2011; Cain et al. 2011). It is found that flexions can be an effective way to study small-scale variations in the projected mass distribution (Goldberg & Bacon 2005; Bacon et al. 2006; Leonard et al. 2009; Er 2012) and to constrain the density slope of dark matter halos (Leonard et al. 2007; Velander et al. 2011).

In this paper, we study how well one can determine the ratio between stellar mass and dark matter halo mass for galaxies by combining shear and flexions. For certain amounts of stellar mass contained in galaxies, we predict theoretical lensing signals using the mass-to-light relation extracted from the Millennium-II simulation (MSII, Boylan-Kolchin et al. 2009) and a semi-analytical galaxy catalog constructed with it (Guo et al. 2011, hereafter G11). Then we perform mock lensing observations using the conditions of future galaxy surveys. For each set of mock observations, the constraints on lensing effects are studied in detail.

The structure of the paper is as follows. In Section 2, we present the basic lensing theory. In Section 3, we describe our simulations. In Section 4, we show the results. The discussion and conclusions are in Section 5. Throughout this paper, we adopt the WMAP-7 cosmology (Komatsu et al. 2011): $\Omega_M = 0.275$, $\Omega_\Lambda = 0.725$ and $\sigma_8 = 0.816$, and write the Hubble constant as $H_0 = 100\,h\,\mathrm{km\,s^{-1}\,Mpc^{-1}}$, where $h = 0.702$.

2 LENSING BASICS

The full formalism described here can be found in Bacon et al. (2006) and Schneider & Er (2008). Throughout the paper, the thin lens approximation is adopted. The dimensionless surface mass density can be written as

$$\kappa(\boldsymbol{\theta}) = \Sigma(\boldsymbol{\theta})/\Sigma_{\mathrm{cr}}, \quad \text{with critical surface mass density} \quad \Sigma_{\mathrm{cr}} = \frac{c^2}{4\pi G}\frac{D_{\mathrm{s}}}{D_{\mathrm{d}}D_{\mathrm{ds}}}, \qquad (1)$$

where D_{s} and D_{d} are the angular diameter distances from source and lens to observer respectively, D_{ds} is the angular distance from lens to the source, and $\Sigma(\boldsymbol{\theta})$ is the surface mass density of the lens. The lensing potential is given by

$$\psi(\theta) = \frac{1}{\pi}\int \kappa(\theta')\ln|\theta - \theta'|\,\mathrm{d}^2\theta'. \qquad (2)$$

The low order image distortion caused by lensing is described by shear $\gamma = \gamma_1 + i\gamma_2$, which transforms a circular source into an elliptical image, where

$$\gamma_1 = \frac{1}{2}(\psi_{11} - \psi_{22}), \qquad\qquad \gamma_2 = \frac{1}{2}(\psi_{12} + \psi_{21}), \qquad (3)$$

and $\psi_{ij} = \partial^2\psi/\partial\theta_i\partial\theta_j$. The next higher-order effect is called the flexion. It includes two components, the first flexion $\mathcal{F}$ and the second flexion $\mathcal{G}$

$$\mathcal{F} = \nabla_{\mathrm{c}}\kappa, \qquad \mathcal{G} = \nabla_{\mathrm{c}}\gamma, \qquad (4)$$

where ∇_c is the complex derivative operator. In polar coordinates, it can be written as

$$\nabla_c = e^{i\phi}\left(\frac{\partial}{\partial\theta} + \frac{i}{\theta}\frac{\partial}{\partial\phi}\right),$$

(5)

where θ is the polar radius and ϕ is the polar angle.

3 METHODOLOGY AND SIMULATION

3.1 Lens Model

We assume that dark matter in halos follows the Navarro-Frenk-White (NFW) (Navarro et al. 1997) profile, which is found to be a good description for halos in both N-body simulations (Springel et al. 2008; Gao et al. 2012) and observations (King et al. 2002; Clowe et al. 2006). The dark matter density can be written as

$$\rho(r) = \frac{\delta_c\rho_{\rm crit}}{(r/r_{\rm s})(1 + r/r_{\rm s})^2},$$

(6)

where $r_{\rm s}$ is the scaling radius, $\rho_{\rm crit}$ is the critical density of the universe and δ_c is a characteristic density which can be written as

$$\delta_c = \frac{200}{3}\frac{c^3}{\ln(1 + c) - c/(1 + c)}.$$

(7)

We use M_{200} (the mass enclosed within radius r_{200}) as the estimator of halo mass, defined as

$$M_{200} = \frac{4\pi}{3}r_{200}^3\rho_{\rm crit}.$$

(8)

The scaling radius $r_{\rm s}$ is related to the halo viral radius r_{200} through the concentration parameter by $c = r_{200}/r_{\rm s}$. Here we adopt the concentration-mass relation given by Bullock et al. (2001). The dimensionless surface density profile of the NFW model is given by Bartelmann (1996),

$$\kappa(x) = 2\kappa_{\rm s}f(x)/(x^2 - 1),$$

(9)

where $\kappa_{\rm s} = \rho_{\rm crit}(z)\delta_c r_{\rm s}/\Sigma_{\rm crit}$, and $x \equiv \xi/r_{\rm s}$ where ξ is the projected distance. The function $f(x)$ is given by

$$f(x) = \begin{cases} 1 - \frac{2}{\sqrt{1-x^2}}\mathrm{arctanh}\left(\sqrt{\frac{1-x}{1+x}}\right), & x < 1, \\ 1 - \frac{2}{\sqrt{x^2-1}}\arctan\left(\sqrt{\frac{x-1}{x+1}}\right), & x > 1. \end{cases}$$

(10)

The analytical form of shear for an NFW halo is given by Wright & Brainerd (2000),

$$\gamma = \kappa_{\rm s}s(x),$$

(11)

where

$$s(x) = \begin{cases} \frac{8\,\mathrm{arctanh}(\sqrt{(1-x)/(1+x)})}{x^2\sqrt{1-x^2}} + \frac{4}{x^2}\ln\left(\frac{x}{2}\right) - \frac{2}{x^2-1} + \frac{4\mathrm{arctanh}(\sqrt{(1-x)/(1+x)})}{(x-1)(1-x^2)^{1/2}}, & x < 1, \\ \frac{8\,\mathrm{arctanh}(\sqrt{(x-1)/(1+x)})}{x^2\sqrt{x^2-1}} + \frac{4}{x^2}\ln\left(\frac{x}{2}\right) - \frac{2}{x^2-1} + \frac{4\mathrm{arctanh}(\sqrt{(x-1)/(1+x)})}{(x-1)^{3/2}}, & x > 1. \end{cases}$$

(12)

According to Equation (4), the first flexion $\mathcal{F}$ can be written as

$$\mathcal{F} = -\frac{2\mathcal{F}_{\rm s}}{(x^2 - 1)^2}\left[2xf(x) - h(x)\right]e^{i\phi},$$

(13)

where $\mathcal{F}_s = \kappa_{\mathrm{s}} D_{\mathrm{l}}/r_{\mathrm{s}}$, and

$$h(x) = \begin{cases} \frac{2x}{\sqrt{1-x^2}}\mathrm{arctanh}\left(\sqrt{\frac{1-x}{1+x}}\right) - \frac{1}{x}, & x < 1 \, , \\ \frac{2x}{\sqrt{x^2-1}}\arctan\left(\sqrt{\frac{x-1}{x+1}}\right) - \frac{1}{x}, & x > 1 \, . \end{cases} \tag{14}$$

The second flexion can be written as

$$\mathcal{G} = 2\mathcal{F}_{\mathrm{s}}\left[\frac{8}{x^3}\ln\left(\frac{x}{2}\right) + \frac{\left(\frac{3}{x}(1-2x^2)+g(x)\right)}{(x^2-1)^2}\right]\mathrm{e}^{3\mathrm{i}\phi} \, , \tag{15}$$

where

$$g(x) = \begin{cases} \left(\frac{8}{x^3} - \frac{20}{x} + 15x\right)\frac{2}{\sqrt{1-x^2}}\mathrm{arctanh}\left(\sqrt{\frac{1-x}{1+x}}\right), & x < 1 \, , \\ \left(\frac{8}{x^3} - \frac{20}{x} + 15x\right)\frac{2}{\sqrt{x^2-1}}\arctan\left(\sqrt{\frac{x-1}{x+1}}\right), & x > 1 \, . \end{cases} \tag{16}$$

Realistically, there is a core instead of a dark matter cusp in a lens galaxy because of the interaction of baryonic matter and dark matter. In this paper, we only consider the lensing signal from a dark matter halo, because the baryonic component only dominates the inner part of the galaxy. At the scale we are concerned with in this work, its contribution to lensing signal is one order of magnitude lower than that of a dark matter halo.

3.2 Simulating Lensing Signals

We perform a series of Monte Carlo simulations to mimic lensing observations. Our lens galaxy catalog is taken from real observations, but the halo mass of each lens is calculated by a semi-analytical method.

First of all, we generate the lens galaxy catalog. For a real observation, it is best to select lens galaxies from a spectroscopic survey, which enables one to determine the precise redshift and environment of the lens galaxies (e.g. Mandelbaum et al. 2005; Yang et al. 2007; Li et al. 2013). In this paper, we extract lens statistics from the SDSS Data Release 7 (DR7) spectroscopic galaxy survey. The group catalog is used here, which is constructed by Yang et al. (2007, SDSSGC, hereafter)[1] to identify the galaxy environment. The SDSSGC is constructed with the adaptive halo-based group finder developed by Yang et al. (2005, 2007) using SDSS galaxies with spectroscopic redshifts in the range of $0.02 \leq z \leq 0.2$. Each galaxy is either assigned to a group or identified as a field galaxy. The stellar mass of an individual galaxy is calculated with its magnitude and colors using the fitting formula derived by Bell et al. (2003). In this work, we focus on field galaxies. A total of 452 209 field galaxies are selected from SDSSGC as our mock sample of lens galaxies. The stellar mass range is $10^9 h^{-1}M_{\odot}$ and $5 \times 10^{11} h^{-1}M_{\odot}$, and the stellar mass distribution of SDSS DR7 field galaxies is shown in Figure 1. The numbers of lens galaxies in different stellar mass bins are listed in Table 1.

Table 1 The Number of Lens Galaxies within Each Stellar Mass Bin

Stellar mass range ($h^{-1}M_{\odot}$)	N_{lens}
1×10^9 – 5×10^9	39 718
5×10^9 – 1×10^{10}	43 695
1×10^{10} – 5×10^{10}	232 569
5×10^{10} – 1×10^{11}	106 964
1×10^{11} – 5×10^{11}	38 263

[1] *http://gax.shao.ac.cn/data/Group.html*

The mass-to-light ratio is taken from the semi-analytical galaxy catalog of G11 and the MSII simulation. MSII simulates evolution of 2160^3 dark matter particles in a $(100\ h^{-1}\ \mathrm{Mpc})^3$ box, providing a detailed mass function to the very low mass end. The G11 semi-analytical model follows galaxy evolution in MSII dark matter halos, and includes prescriptions for radiative cooling, star formation, metal enrichment, supernova feedback, active galactic nucleus feedback as well as interactions between galaxies after halo merging, providing predictions that reasonably agree with observed galaxy abundances as a function of stellar mass, luminosity, star formation rate, color, morphology, gas content and metallicity. We draw the relation between mean dark matter mass and stellar mass from this catalog and use it to calculate the halo mass of our mock lens galaxies.

Second, we randomly place the source galaxies in the lens plane. We consider a source density of $60\ \mathrm{arcmin}^{-2}$, which is comparable to the expected survey depth for next generation lensing surveys such as Euclid[2] and LSST[3]. The lenses are fixed at $z_d = 0.1$, which is the approximate mean redshift of galaxies in the SDSS spectroscopic catalog. The sources are at redshift $z_s = 1$, which is the expected mean redshift of next generation lensing surveys.

At each source position, the mock weak lensing signal is given by:

$$\gamma_{\mathrm{sim}} = \gamma_0 + N_\gamma, \tag{17}$$
$$\mathcal{F}_{\mathrm{sim}} = \mathcal{F}_0 + N_{\mathcal{F}}, \tag{18}$$
$$\mathcal{G}_{\mathrm{sim}} = \mathcal{G}_0 + N_{\mathcal{G}}, \tag{19}$$

where γ_{sim}, $\mathcal{F}_{\mathrm{sim}}$ and $\mathcal{G}_{\mathrm{sim}}$ are the simulated weak lensing signals of shear, flexion $\mathcal{F}$ and flexion $\mathcal{G}$. γ_0, F_0 and G_0 are the theoretical predictions, and N_γ, $N_{\mathcal{F}}$ and $N_{\mathcal{G}}$ are their respective noises.

The lensing observation noise may arise from the intrinsic shape noise and measurement noise (e.g. photon noise, an inaccurate point spread function and pixelization effects etc). For shear, measurement noise is relatively less important, and ranges from 0.05 to 0.4, depending on the luminosity of the source galaxies (Mandelbaum et al. 2005). For next generation surveys, the angular resolution and survey depth will significantly improve, thus measurement noise is expected to be even smaller. Throughout this paper, we only consider the error for shear σ_γ, which is due to the intrinsic shape distribution, and we use $\sigma_\gamma = 0.3$ (Kitching et al. 2012; Rowe et al. 2012).

The flexion noises are however more complicated than that of shear. Only intrinsic flexions are used as noise sources in previous studies. Recently, Rowe et al. (2012) claimed that the noise of flexions can be dominated by pixelization effects, e.g. readout noise or finite photon number counts, and the signal-to-noise of flexion is too low to provide useful information. This is, however, based on the method of shapelet flexion estimation which was originally developed for shear measurement. Improvement in facilities (with better CCD readout or smaller pixels) and modification of image analysis methods may reduce this noise in the future. In this paper, we will use the model given in Rowe et al. (2012) as an upper limit on measurement noise.

Therefore, two noise models for flexion are employed here. In model 1, we assume that there is only intrinsic shape noise ($N_{\mathrm{i},\mathcal{F}}$ and $N_{\mathrm{i},\mathcal{G}}$) with $\sigma_{\mathcal{F}} = 0.03$ and $\sigma_{\mathcal{G}} = 0.04$ (Goldberg & Bacon 2005). In model 2, the noise is the sum of intrinsic shape noise and measurement noise ($N_{\mathrm{m},\mathcal{F}}$ and $N_{\mathrm{m},\mathcal{G}}$)

$$N_{\mathcal{F}} = N_{\mathrm{i},\mathcal{F}} + N_{\mathrm{m},\mathcal{F}}, \tag{20}$$
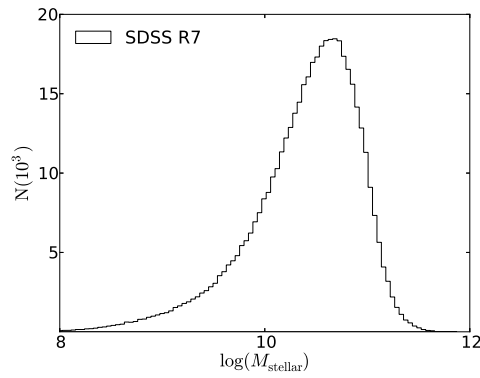$$N_{\mathcal{G}} = N_{\mathrm{i},\mathcal{G}} + N_{\mathrm{m},\mathcal{G}}. \tag{21}$$

For simplicity, we assume that the measurement noise follows a Gaussian distribution with standard deviation $\mathrm{STD}_{\mathrm{m}}$ given by (Rowe et al. 2012)
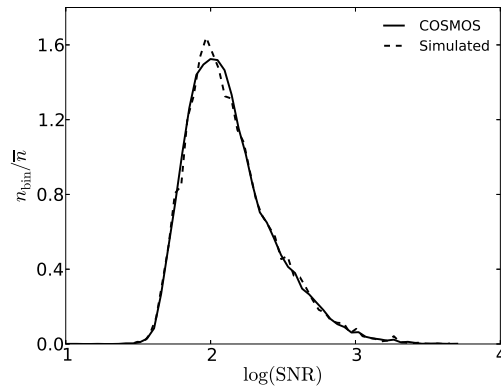
$$\mathrm{STD}_{\mathrm{m}} = A_{100}(\mathrm{SNR}/100)^b. \tag{22}$$

---

[2] *sci.esa.int/euclid/*

[3] Large Synoptic Survey Telescope, *http://www.lsst.org/lsst/scibook*

Fig. 1 Distribution of stellar mass for field galaxies in SDSSGC.

Fig. 2 The distribution of SNRs for our simulated sources and that of COSMOS. The dashed line shows the normalized distribution function of the SNR for our mock sources. The solid line shows the normalized distribution function of sources in COSMOS.

For flexion $\mathcal{F}$, $\{A_{100}, b\} = \{0.33, -0.83\}$, and for flexion $\mathcal{G}$, $\{A_{100}, b\} = \{1.52, -0.81\}$. In our simulations, we assume the supernovae remnant (SNR) distribution of sources follows that of the HST COSMOS survey[4]. We show the source SNR distribution of the COSMOS survey and that of our mock source catalog in Figure 2.

4 RESULTS

We first show the simulated lensing signals. Lens galaxies are binned in narrow ranges of stellar mass. For each bin, we stack lens-source systems and calculate the average shear (flexions) as a function of separation between source and lens.

In Figure 3, we show the lensing signals of different stellar mass bins and of different noise models. Solid curves show the input model of shear, flexion $\mathcal{F}$ and flexion $\mathcal{G}$, while points with errorbars show the simulated signals with 1σ uncertainties. In the left panels, we show the result with only intrinsic noise. We find that in the limit of intrinsic noise, one will be able to measure

---

[4] *http://cosmos.astro.caltech.edu/astronomer/hst.html*
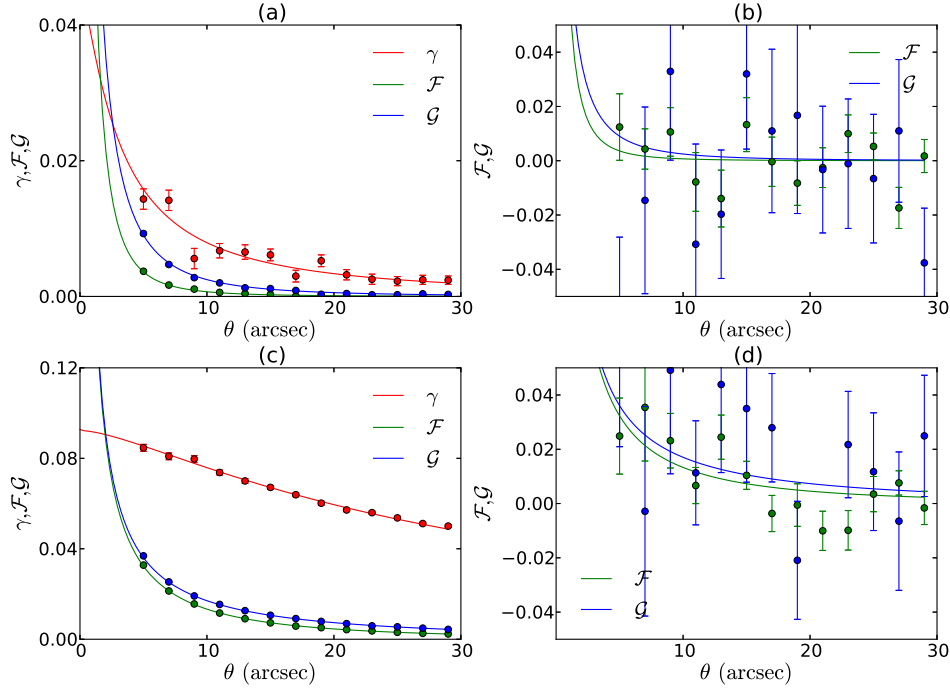
Fig. 3 Input model and simulated lensing signals. Top panels show the results of the galaxies within stellar mass bin $[10^9, 5 \times 10^9]\ h^{-1}M_\odot$. Bottom panels show the results of the $[10^{11}, 5 \times 10^{11}]$ $h^{-1}M_\odot$ bin. The signals are plotted as a function of separation between source and lens. Solid curves show the input model of shear (*red*), flexion $\mathcal{F}$ (*green*) and flexion $\mathcal{G}$ (*blue*). Points with errorbars show the simulated signals with 1σ uncertainties of shear (*red*), flexion $\mathcal{F}$ (*green*) and flexion $\mathcal{G}$ (*blue*). In the left panels, we use noise model 1 for flexion $\mathcal{F}$ and flexion $\mathcal{G}$, while in the right panels we use noise model 2. The unit of flexion is arcsec^{-1}.

correlation of both galaxy-shear and galaxy-flexion with great precision using a next generation survey. In the right panels, we also show the simulated flexions with noise model 2. Even for future surveys, the noise described in Rowe et al. (2012) is still significant compared to the flexion signal.

Note that, if the source is too close to the lens, the light from the lens may pollute the lensing signal and introduce bias. In this paper, we only consider lens-source pairs with separation larger than $5''$.

We apply a Bayesian framework to study the simulated maps. The maps contain tangential shear and two radial flexions. We assume that the noises of shear and flexions are uncorrelated. The shear noise follows a Gaussian distribution with mean zero and $\sigma_\gamma = 0.3$. The likelihood is the conditional probability of the data given the halo parameters. For example, the likelihood function for the first flexion is

$$\mathcal{L}_\mathcal{F} = \frac{1}{\sqrt{2\pi}\sigma_\mathcal{F}} \exp\left(-\frac{(\mathcal{F}_r - \mathcal{F}_{t,r})^2}{2\sigma_\mathcal{F}^2}\right), \qquad (23)$$

where $\mathcal{F}_r$ is the radial component of the mock data, $\mathcal{F}_{t,r}$ is that of the theoretical prediction for a given model, and $\sigma_\mathcal{F}$ is the standard deviation of the noise. The joint likelihood can be written as

$$\mathcal{L} = \mathcal{L}_\mathcal{F}\mathcal{L}_\mathcal{G}\mathcal{L}_\gamma, \qquad (24)$$
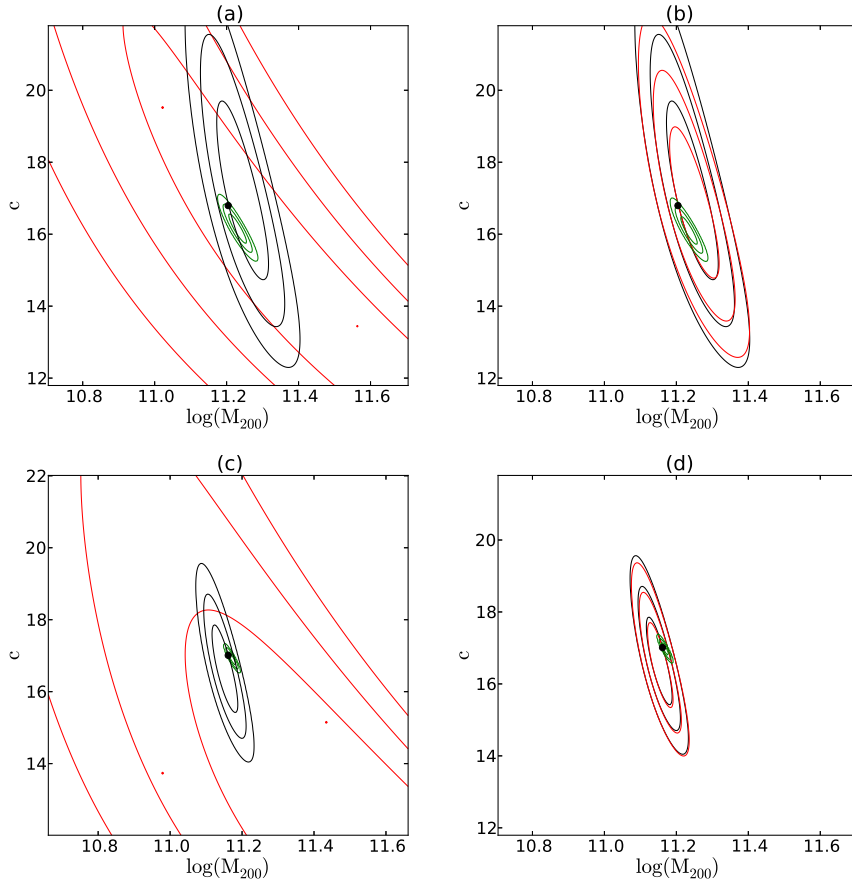
Fig. 4 Parameter constraints using shear, flexion $\mathcal{F}$ and flexion $\mathcal{G}$ with different noise models. In the left panels, we show the parameter constraints from shear and flexions separately. The black contours are the constraints from shear, while the other ones are constraints from combining $\mathcal{F}$ and $\mathcal{G}$. The green contours are for flexion noise model 1 and the red ones are for model 2. In the right panel, the contours show the joint fitting using both simulated shear and flexions. The green contours are for flexion noise model 1 and the red ones for model 2. For comparison, we also plot constraints from only shear with a black contour. The contour levels show the 67.8%, 95.4% and 99.7% confidence limits. The source density of the simulation is $n_{\rm bg} = 10 \ {\rm arcmin}^{-2}$ for the upper panels and $n_{\rm bg} = 60 \ {\rm arcmin}^{-2}$ for the lower panels. The black point shows the mean M_{200} and concentration of the input lens.

where $\mathcal{L}_{\mathcal{G}}$ and $\mathcal{L}_{\gamma}$ are the likelihoods of flexion $\mathcal{G}$ and shear, which have the same form as Equation (23).

The theoretical predictions are calculated using the formula in Section 3 and two parameters are varied: halo mass and concentration. We use flat priors for the two parameters.

In Figure 4, we show the result for galaxies in stellar mass bin $[10^9, 5 \times 10^9] \ h^{-1} M_{\odot}$. The contour levels show the 67.8%, 95.4% and 99.7% confidence intervals. The mean values of the input lens systems are shown with black solid points in each panel. In the left panels, we show the parameter constraints from shear and flexions separately. We find that, in the limit of intrinsic
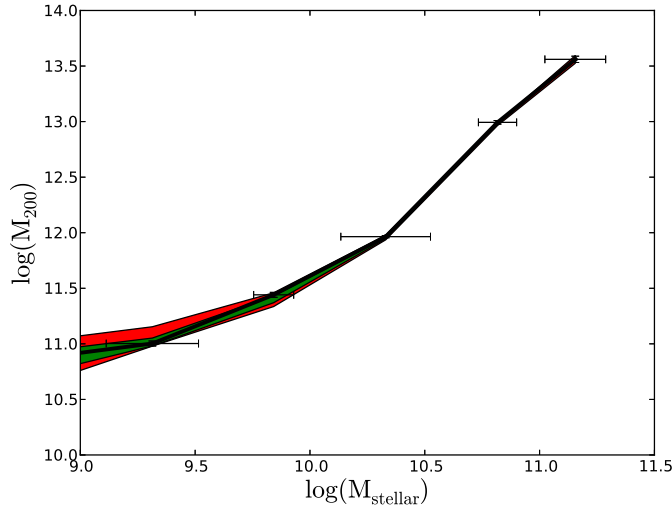
Fig. 5 Constraints on the relation between stellar mass and halo mass. The black curve shows the input model. The errorbars represent 1σ uncertainties of M_{200} and $M_{\rm stellar}$ in each stellar mass range from the input galaxy catalogs. The shadow shows the 1σ confidence interval of M_{200} when combining simulated shear and flexions with noise model 1 (*green*) and model 2 (*red*), respectively.

noise, flexions provide tighter constraints on both halo mass and concentration. For galaxies in stellar mass bin $[10^9, 5 \times 10^9] \; h^{-1}M_\odot$, both parameters can be determined to 10% accuracy by only using the flexion measurement. However, if the noise follows the form described by Rowe et al. (2012), flexions can only provide very weak constraints.

The shear and flexions have different dependences on halo parameters. As is shown in Figure 3, the signals from flexions are much steeper in the inner region and drop quickly when the radii become larger. We expect flexions to be more sensitive to the inner mass distribution of dark matter halos. Combining the two measurements should help to break the parameter degeneracy between mass and concentration. In the right panels, we show the results of the joint fitting that uses both simulated shear and flexions. We find that the orientations of confidence contours from shear and flexions are indeed misaligned. However, since the relative intrinsic noise of flexions is smaller than shear, in the limit of intrinsic noise, the constraints on parameters mainly come from flexions. On the other hand, in the case of flexion noise model 2, the parameter constraints are dominated by shear. Combining the flexion measurement shrinks the confidence contour by about 5%. For comparison, we also show the constraints with source number density of $10 \; {\rm arcmin}^{-2}$.

Finally, we analyze lensing effects for a wide range of galaxies, and show constraints on the relation between stellar mass and halo mass.

In Figure 5, the black curve shows this relation for our simulation, and the errorbars represent 1σ variation. The shadows show the 1σ confidence interval combining shear signals and flexions with different noise models. Obviously, for both cases of noise, future lensing observations can put strong constraints on the relation between stellar mass and dark matter mass. Even for the worst case of flexion noise, the average halo mass can be determined to a precision of 0.1 dex for galaxy bins with stellar mass larger than $10^9 \; h^{-1}M_\odot$ with galaxy-galaxy lensing. If the flexion measurement noise can be well calibrated, the constraints on the relation between galaxy mass and halo mass will be improved by a factor of two.

5 SUMMARY

In this paper, we explore the potential of constraining the relation between galaxy stellar mass and halo mass using shear and flexions. We use the SDSS catalog and a semi-analytical model to generate mock lens samples, and use a suite of Monte Carlo simulations to generate weak lensing observations with different noise models. Using mock data, we find that the inclusion of flexions can improve the estimate of foreground halo parameters, although the details strongly depend on the noise model.

Two flexion noise models are used in this paper, which are roughly the upper and lower limit of flexion noise. In one noise model, we use only intrinsic noise. In the other case, we add a conservative measurement of the noise model based on shapelets. We find that adopting a joint fit with shear and flexions breaks part of the degeneracy between halo mass and concentration parameter. Even in the worst case of noise, the joint fit helps to shrink confidence contours by 5%.

In the limit of intrinsic noise, we find that, with next generation lensing surveys, both shear and flexions are promising tools to study the correlation between a galaxy and its associated dark matter as a function of stellar mass in the galaxy. However, if the level of systematic error is as described in Rowe et al. (2012), flexions will not be able to put tight constraints on parameters describing the dark matter halo, even with the next generation of lensing observations. The noise measurement from flexions is a critical problem. Advanced image analysis will be useful for reducing measurement noise and to obtain better constraints on dark matter halos.

References

Bacon, D. J., Goldberg, D. M., Rowe, B. T. P., & Taylor, A. N. 2006, MNRAS, 365, 414
Bartelmann, M. 1996, A&A, 313, 697
Bell, E. F., McIntosh, D. H., Katz, N., & Weinberg, M. D. 2003, ApJS, 149, 289
Boylan-Kolchin, M., Springel, V., White, S. D. M., Jenkins, A., & Lemson, G. 2009, MNRAS, 398, 1150
Brainerd, T. G., Blandford, R. D., & Smail, I. 1996, ApJ, 466, 623
Bullock, J. S., Kolatt, T. S., Sigad, Y., et al. 2001, MNRAS, 321, 559
Cacciato, M., van den Bosch, F. C., More, S., et al. 2009, MNRAS, 394, 929
Cain, B., Schechter, P. L., & Bautz, M. W. 2011, ApJ, 736, 43
Clowe, D., Bradač, M., Gonzalez, A. H., et al. 2006, ApJ, 648, L109
Cole, S., Lacey, C. G., Baugh, C. M., & Frenk, C. S. 2000, MNRAS, 319, 168
Croton, D. J., Springel, V., White, S. D. M., et al. 2006, MNRAS, 365, 11
Er, X. 2012, arXiv:1212.3907
Gao, L., Navarro, J. F., Frenk, C. S., et al. 2012, MNRAS, 425, 2169
Gillis, B. R., Hudson, M. J., Erben, T., et al. 2013, arXiv:1301.7421 (MNRAS in press)
Goldberg, D. M., & Bacon, D. J. 2005, ApJ, 619, 741
Guo, Q., White, S., Boylan-Kolchin, M., et al. 2011, MNRAS, 413, 101 (G11)
Hawken, A. J., & Bridle, S. L. 2009, MNRAS, 400, 1132
Heymans, C., Grocutt, E., Heavens, A., et al. 2013, arXiv:1303.1808
Hoekstra, H., Franx, M., Kuijken, K., Carlberg, R. G., & Yee, H. K. C. 2003, MNRAS, 340, 609
Hoekstra, H., Yee, H. K. C., & Gladders, M. D. 2004, ApJ, 606, 67
Hudson, M. J., Gwyn, S. D. J., Dahle, H., & Kaiser, N. 1998, ApJ, 503, 531

Johnston, D. E., Sheldon, E. S., Tasitsiomi, A., et al. 2007, ApJ, 656, 27

Kang, X., Jing, Y. P., Mo, H. J., & Börner, G. 2005, ApJ, 631, 21

Katz, N., Weinberg, D. H., & Hernquist, L. 1996, ApJS, 105, 19

Kauffmann, G., White, S. D. M., & Guiderdoni, B. 1993, MNRAS, 264, 201

Kauffmann, G., White, S. D. M., Heckman, T. M., et al. 2004, MNRAS, 353, 713

Kilbinger, M., Fu, L., Heymans, C., et al. 2013, arXiv:1212.3338 (MNRAS in press)

King, L. J., Clowe, D. I., & Schneider, P. 2002, A&A, 383, 118

Kitching, T. D., Balan, S. T., Bridle, S., et al. 2012, MNRAS, 423, 3163

Komatsu, E., Smith, K. M., Dunkley, J., et al. 2011, ApJS, 192, 18

Leonard, A., Goldberg, D. M., Haaga, J. L., & Massey, R. 2007, ApJ, 666, 51

Leonard, A., King, L. J., & Wilkins, S. M. 2009, MNRAS, 395, 1438

Li, R., Mo, H. J., Fan, Z., Yang, X., & Bosch, F. C. v. d. 2013, arXiv:1210.2480 (MNRAS in press)

Li, R., Mo, H. J., Fan, Z., et al. 2009, MNRAS, 394, 1016

Mandelbaum, R., Seljak, U., Cool, R. J., et al. 2006, MNRAS, 372, 758

Mandelbaum, R., Seljak, U., Hirata, C. M., et al. 2008, MNRAS, 386, 781

Mandelbaum, R., Tasitsiomi, A., Seljak, U., Kravtsov, A. V., & Wechsler, R. H. 2005, MNRAS, 362, 1451

McKay, T. A., Sheldon, E. S., Racusin, J., et al. 2001, arXiv:astro-ph/0108013

Navarro, J. F., Frenk, C. S., & White, S. D. M. 1997, ApJ, 490, 493

Pearce, F. R., Thomas, P. A., Couchman, H. M. P., & Edge, A. C. 2000, MNRAS, 317, 1029

Rowe, B., Bacon, D., Massey, R., et al. 2012, arXiv:1211.0966

Schneider, P., & Er, X. 2008, A&A, 485, 363

Sheldon, E. S., Johnston, D. E., Frieman, J. A., et al. 2004, AJ, 127, 2544

Simon, P., Erben, T., Schneider, P., et al. 2013, arXiv:1301.1863 (MNRAS in press)

Somerville, R. S., & Primack, J. R. 1999, MNRAS, 310, 1087

Springel, V. 2005, MNRAS, 364, 1105

Springel, V., Wang, J., Vogelsberger, M., et al. 2008, MNRAS, 391, 1685

Tyson, J. A., Valdes, F., Jarvis, J. F., & Mills, A. P., Jr. 1984, ApJ, 281, L59

van den Bosch, F. C., Abel, T., Croft, R. A. C., Hernquist, L., & White, S. D. M. 2002, ApJ, 576, 21

Velander, M., Kuijken, K., & Schrabback, T. 2011, MNRAS, 412, 2665

White, S. D. M., & Frenk, C. S. 1991, ApJ, 379, 52

White, S. D. M., & Rees, M. J. 1978, MNRAS, 183, 341

Wright, C. O., & Brainerd, T. G. 2000, ApJ, 534, 34

Yang, X., Mo, H. J., & van den Bosch, F. C. 2006, ApJ, 638, L55

Yang, X., Mo, H. J., van den Bosch, F. C., & Jing, Y. P. 2005, MNRAS, 356, 1293

Yang, X., Mo, H. J., van den Bosch, F. C., et al. 2007, ApJ, 671, 153